Feedback phase correction of Bessel beams in confocal line light-sheet microscopy: a simulation study

S. Hoda Moosavi, Cristian Gohn-Kreuz, and Alexander Rohrbach*

Laboratory for Bio- and Nano-Photonics, Department of Microsystems Engineering-IMTEK, University of Freiburg, Georges Köhler Allee 102, 79110 Freiburg, Germany

*Corresponding author: rohrbach@imtek.de

Received 13 June 2013; revised 11 July 2013; accepted 14 July 2013; posted 15 July 2013 (Doc. ID 192292); published 9 August 2013

Confocal line detection has been shown to improve contrast in light-sheet-based microscopy especially when illuminating the sample by Bessel beams. Besides their self-reconstructing capability, the stability in propagation direction of Bessel beams allows to block the unwanted emission light from the Bessel beam's ring system. However, due to phase aberrations induced especially at the border of the specimen, Bessel beams may not propagate along lines parallel to the slit detector. Here we present a concept of how to correct the phase of each incident Bessel beam such that the efficiency of confocal line detection is improved by up to 200%–300%. The applicability of the method is verified by the results obtained from numerical simulations based on the beam propagation method.

OCIS codes: (180.0180) Microscopy; (180.5810) Scanning microscopy; (070.3185) Invariant optical fields; (070.6120) Spatial light modulators; (070.7345) Wave propagation; (080.5692) Ray trajectories in inhomogeneous media.

http://dx.doi.org/10.1364/AO.52.005835

1. Introduction

Light-sheet-based microscopy (LSBM) provides wide-field optical sectioning in large samples by exciting fluorescence only in a thin volume around the focal plane of the detection optics. The sample is typically illuminated by a separate optical system oriented orthogonally to the detection optical axis [1,2]. An optimal image quality is obtained for very thin light sheets that homogeneously illuminate the imaged plane. However, the defined shape of a light sheet is strongly degraded due to diffraction and scattering of illumination light by the sample [3].

A light sheet with advantageous properties can be generated by scanning a Bessel beam across the field of view in the focal plane. Due to the self-reconstructing capability of Bessel beams, beam spreading and scattering are reduced, resulting in a more homogeneous light sheet and increased penetration depth [4]. This allows to examine details deeper within large, scattering samples. Bessel beams can be generated very flexibly by using spatial light modulators (SLMs), placed in a conjugate plane to the illumination objective's (IO's) focal plane. The thin central lobe of a Bessel beam, however, is surrounded by an extended ring system that carries a significant amount of energy. When the beam is scanned across the field of view, the images of the rings smear out and thereby effectively create a light sheet much thicker than the central lobe. This averaging effect results in images with reduced contrast [5,6]. As the energy in the rings is crucial to the beam's self-reconstruction ability, it cannot be reduced. However, it is possible to block the (fluorescence) light emitted from the ring system by using a slit detector, which enables confocal line detection [7–9]. A sketch of this principle is given in Fig. 1. This

1559-128X/13/235835-08$15.00/0

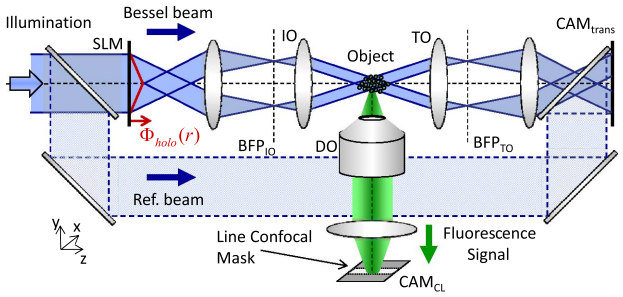

Fig. 1. Interferometric setup scheme. The illumination beam is split up into a reference beam and the object beam (blue colors). An SLM modulates a conical phase to the beam, resulting in a Bessel beam (IO, illumination objective; TO, transmission objective). The interference intensity is detected by a camera (CAM_{trans}). Fluorescence emitted from the object (green colors) is imaged by a detection objective (DO) onto a line-confocal camera (CAM_{CL}).

method has been shown to be especially advantageous to Bessel beams, which reveal an inherent propagation stability along a specific direction that is significantly better than that of a conventional Gaussian-shaped laser beam. In this way resolution and contrast can be significantly increased.

However, due to phase aberrations induced especially at the borders of large specimen, such as embryos [10], cell clusters [11], or small plants [12], Bessel beams may be deflected as well. The refraction due to a jump in refractive index between the surrounding medium, typically an agarose gel, and the higher refractive index of the specimen can result in the deviation of the Bessel beam's main maximum of some degrees. Very often the border of 0.1–0.5 mm large objects is of spherical shape, such that each incident Bessel beam is refracted under a different (mean) angle.

In this study we describe a method of how to correct the phase of Bessel beams incident on a near spherical object of unknown mean radius and mean refractive index by analyzing the transmitted laser light. Among other methods, the angular deviation of the Bessel beam's main intensity maximum relative to the illumination optical axis can be measured interferometrically in a plane behind the object. Using a small number of reference measurements of the spectrum of outgoing beams, the spectrum of all incident beams can be corrected in such a way that the main lobe of the Bessel beam inside the object propagates parallel to the slit detector. In this way the confocal line detection principle can be applied very efficiently, resulting in a more homogeneous sample illumination across the field of view and a better localized illumination in the back part of the sample. Our concept is proven by numerical computer simulations based on the beam propagation method (BPM) [13], where a large number of phase-corrected Bessel beams propagate through a large homogeneous sphere and nonhomogenous cluster of cells.

Section 2 of this paper presents a possible setup to retrieve the phase of each transmitted beam by interferometry. Section 3 introduces the basic principles of beam propagation through two different refractive index model distributions. Section 4 explains the benefits and the problems with confocal line detection in LSBM. Section 5 presents a method to correct for the propagation angle inside the sample based on geometrical optics. In Section 6 we discuss the transfer to wave optics and phase retrieval by two beam interference. The main results of this study are presented in Section 7.

2. Setup Scheme

Our imaging simulation is based on a standard light-sheet-based microscope using laterally scanned illumination beams [4,10]. As illustrated in Fig. 1, an SLM modulates the phase of the incident illumination beam to $\phi_{\mathrm{holo}}(x,y)$, which is conical in the case for a Bessel beam. The Bessel beam (in blue colors) illuminates the object from the side. While the Bessel beam propagates through the labeled object—a cluster of spheres—fluorescence is emitted along the illumination beam and detected by $\mathrm{NA_{DO}} = 1.0$ detection objective (DO). The camera (CAM_{CL}) in the image plane is either a 2D camera with a rolling line confocal mask or a 1D line camera with additional descanning mirrors. By using this slit detection principle, only fluorescence along the central main lobe of the Bessel beam is detected and fluorescence excited by the Bessel ring system is blocked. The numerical apertures of the IO and transmission objective (TO) are assumed to have $\mathrm{NA_{IO}} = \mathrm{NA_{TO}} = 0.35$.

While propagating through the object, single plane wave components of the Bessel beam are deflected by the object, which results in a deviation of the conical phase behind the object. This phase deviation can be determined to a good approximation by phase-shifting interferometry with a reference beam as indicated in principle in Fig. 1. The three or four different interference intensities are measured by a camera (CAM_{trans}) and analyzed by a computer, and a corrected phase $\Delta\phi(x,y)$ is modulated onto the incident beam by the SLM to improve the propagation behavior of each single illumination beam. As we will show later, the main lobe of the Bessel beam has to propagate parallel to the slit orientation on the camera CAM_{CL} to produce a high-quality image with a homogeneous object illumination in the focal plane of the DO.

3. Beam Propagation through an Inhomogeneous Medium

A series of illumination beams displaced in x direction and propagating through an extended object along the z direction forms a light sheet in the xz plane, which is then imaged onto the camera along the y direction (see Fig. 1). To obtain the intensities inside and behind the inhomogeneous object, we numerically calculate the electric field by using a scalar BPM [13].

Here the angular spectrum of the electric field at a distance $z + dz$ propagating through the sample can be described by

$$\tilde{E}(k_x,k_y,z+dz)=\mathrm{FT}[E(x,y,z)\cdot e^{-ik_0\cdot\delta n(x,y,z)\cdot dz}]\cdot e^{-i\cdot dz\cdot\sqrt{(k_0 n_m)^2-k_x^2-k_y^2}}. \quad (1)$$

FT[…] denotes the Fourier transform in x and y, and $k_0=2\pi/\lambda$ the vacuum wave number. The space-dependent refractive index $n(\mathbf{r})=n_m+\delta n(\mathbf{r})$ changes by $\delta n(\mathbf{r})<\delta n_{\max}$ around the mean value n_m, typically defined by the index of the scatterer's environment.

A. Refractive Index Distribution

In this paper we used two different refractive index distributions with $n_m=1.33$ and $\delta n=0.08$. The first one is that of a large centered sphere (sp) of radius $R_{\mathrm{sp}}=23.5$ μm such that

$$n_{\mathrm{sp}}(x,y,z)=n_m+\delta n\cdot\mathrm{step}\left(R_{\mathrm{sp}}-\sqrt{x^2+y^2+z^2}\right), \quad (2)$$

where $\mathrm{step}(r)=1$ if $r>0$ (and 0 otherwise) designates the Heaviside step function. The other index distribution is that of a cell cluster, which also has a radius of $R_{\mathrm{sp}}=R_{\mathrm{cc}}=23.5$ μm but contains $N=22{,}606$ single cells (sc). These cells consist of a shell with an outer radius $R_{\mathrm{sc}}=1.1$ μm and inner radius $0.85\cdot R_{\mathrm{sc}}$ reflecting the increased index $n=1.33+0.08$ of the cell membrane and actin cortex relative to a mean index $n=1.33+{}^2/_3\cdot 0.08$ of the cell plasma (the nucleus is disregarded).

The cells are arranged in arbitrary order inside a spherical volume:

$$n_{\mathrm{cc}}(\mathbf{r})=n_m+\partial n\cdot\sum_{j=1}^{N}\left[\mathrm{step}(R_{\mathrm{sc}}-|\mathbf{r}-\mathbf{r}_j|)-\frac{1}{3}\mathrm{step}(0.85R_{\mathrm{sc}}-|\mathbf{r}-\mathbf{r}_j|)\right]. \quad (3)$$

The volume fraction of the cells inside the spherical volume cluster is 85%, leaving small volume gaps between the cells with index $n_m=1.33$. Figure 2 displays the volume-rendered model of the index distribution $\delta n(\mathbf{r})$ defined in Eq. (3). The inset of Fig. 2(c) depicts a single cell, revealing the shell-like structure of a single cell with a core and a cladding. The projection of the refractive index distribution along the propagation direction—the optical path length OPL(x)—is plotted for both the large sphere and the cell cluster, demonstrating that the large sphere is a simplified model of the cell cluster. The mean free path lengths of the photons (corresponding to the penetration depth of the illumination beam) are several hundred micrometers as measured recently for different illumination beams propagating through cancer cell spheroids [14].

B. Bessel Beam Propagation

The angular spectrum of a Bessel beam $\tilde{E}(k_x,k_y,z=-24$ μm) in front of the object (corresponding to the field at $\mathrm{BFP_{IO}}$) has an annular shape, as shown by the red ring on the left of Fig. 3(a). The ring thickness in the k_x,k_y plane determines the relative amount of energy in the main lobe of the Bessel beam and thereby the self-reconstruction ability and the depth of field, which must be adapted to the object extension. The resulting intensity $I(x,z)$ along the propagation direction as visible in the focal plane of the DO is shown in the middle, whereas the phase $\phi_{\mathrm{holo}}(x,y)$ generated by the SLM is shown on the right of Fig. 3(a). In Fig. 3(b) the corresponding angular spectrum, the intensity in the DO focal plane, and the phase profile are shown for a tilted Bessel beam.

Whereas the intensity cross section and the angular spectrum of a Bessel beam remain approximately constant during free space propagation, as illustrated in Fig. 3, the Bessel beam's ring spectrum spreads out during propagation through an inhomogeneous medium such as a cluster of cells. Figure 4(a) shows the cross section of the logarithmic angular spectrum intensity $\tilde{I}(k_x,0,z)=|\tilde{E}(k_x,0,z)|^2$ as a

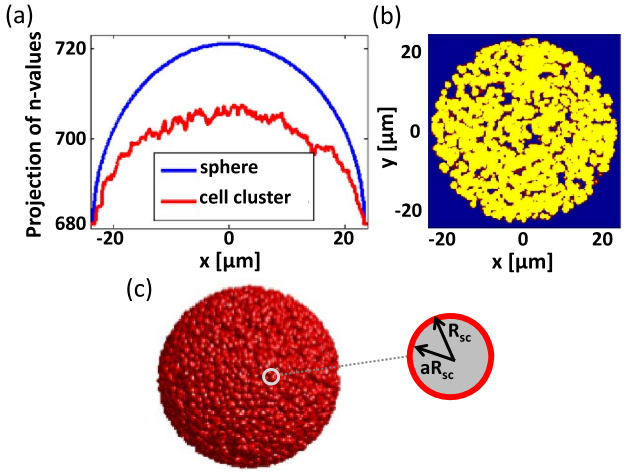

Fig. 2. (a) Comparison of refractive index projections in a cell cluster and in a large homogeneous sphere, (b) cross section through the refractive index distribution of the cell cluster, and (c) volume-rendered cell cluster and shell-like constitution of a single cell with outer radius R_{sc} and inner radius $a\cdot R_{\mathrm{sc}}$ ($a=0.85$).

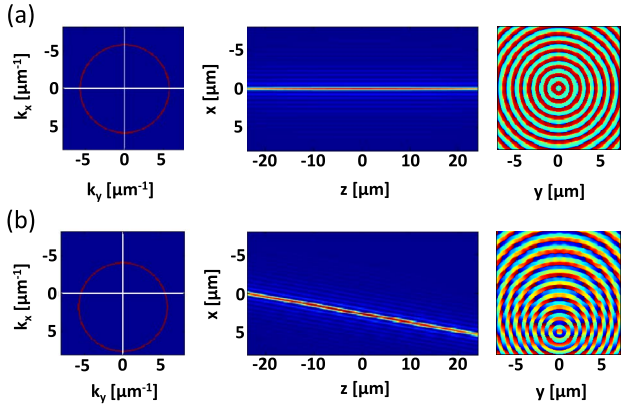

Fig. 3. (a) Nontilted and (b) tilted Bessel beam intensity cross sections and phase diagrams.

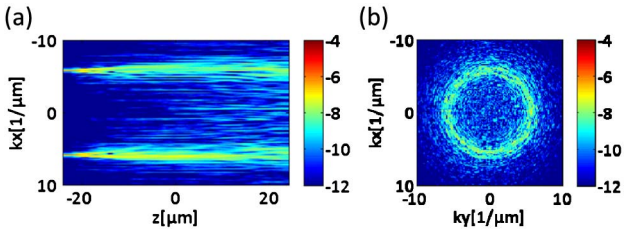

Fig. 4. Power spectrum of Bessel beam incident on a spherical cell cluster. (a) Along the propagation direction, $\log(I(k_x,z))$ and (b) behind the spherical cell cluster, $\log(I(k_x,k_y))$.

function of the propagation distance. Here, the ring spectrum with initial focusing angle $k_x = 2\pi/\lambda \cdot \sin(\theta) \approx 7/\mu\text{m}$ corresponding to $\text{NA}_{\text{IO}} = 1 \cdot \sin(20.5°) = 0.35$ broadens due to scattering at a cluster of cells. Figure 4(b) shows the logarithmic power spectrum $\tilde{I}(k_x,k_y,z_{\text{end}})$ behind the cluster of spheres, which reveals the distorted ring spectrum of a Bessel beam.

4. Confocal Line Detection

In the following we will designate the intensity distribution of a single beam $h_{\text{SB}}(x-b_x,y,z) = |E(x-b_x,y,z)|^2$. This beam is displaced by b_x and propagated through an inhomogeneous medium according to Eq. (1). By adding up all displaced beams h_{SB} along the x direction, one can generate a scanned light sheet $h_{\text{scan}}(\mathbf{r}) = \int h_{\text{SB}}(\mathbf{r}-\mathbf{b}_x)\text{d}b_x$. The resulting 3D image of the light-sheet $p_{\text{LS}}(\mathbf{r})$ is generated by the fluorophore distribution $C(\mathbf{r})$ multiplied by the illumination intensity $h_{\text{scan}}(\mathbf{r})$) and then convolved (symbol $*$) with the detection point-spread function $h_{\text{det}}(\mathbf{r})$:

$$\begin{aligned} p_{\text{LS}}(\mathbf{r}) &= \left(C(\mathbf{r}) \cdot \int h_{\text{SB}}(\mathbf{r}-\mathbf{b}_{\text{x}})\text{d}\mathbf{b}_{\text{x}}\right) * h_{\text{det}}(\mathbf{r}) \\ &\approx \text{C}_0 \cdot \int h_{\text{SB}}(\mathbf{r}-\mathbf{b}_{\text{x}})\text{d}\mathbf{b}_{\text{x}} \\ &= \text{C}_0 \cdot h_{\text{scan}}(\mathbf{r}). \end{aligned} \tag{4}$$

In the second line we have assumed the fluorophore distribution $C(\mathbf{r}) = C_0$ to be homogeneous all over the sample and the detection point-spread function $h_{\text{det}}(\mathbf{r})$ to be narrow in all three dimensions, such that its influence can be disregarded. In the case of confocal line detection, the fluorophore distribution is convolved, with a system point-spread function [9] that can be approximated by $h_{\text{CL}}(\mathbf{r}) \approx h_{\text{SB}}(\mathbf{r}) \cdot h_{\text{det}}(\mathbf{r})$, such that the confocal line image $p_{\text{CL}}(\mathbf{r})$ is given by

$$\begin{aligned} p_{\text{CL}}(\mathbf{r}) &\approx \int C(\mathbf{r}) * [h_{\text{SB}}(\mathbf{r}-\mathbf{b}_{\text{x}}) \cdot h_{\text{det}}(\mathbf{r})]\text{d}\mathbf{b}_x \\ &\approx \text{C}_0 \cdot \int h_{\text{CL}}(\mathbf{r}-\mathbf{b}_x)\text{d}\mathbf{b}_x. \end{aligned} \tag{5}$$

The beneficial effect of confocal line detection especially for Bessel beams is illustrated in Fig. 5, where three xy cross sections (at $z = 0$) of the 3D images are shown; they are computed according to Eqs. (4) and (5). Whereas in Fig. 5(a) the effect of the Bessel beam's ring system is clearly visible in the conventional imaging mode and the optical sectioning is poor, this effect is strongly suppressed and results in a very thin light sheet and excellent optical sectioning when using confocal line detection {see Figs. 5(b) and 5(c), as well as [15] and sectioning references therein}.

However, the principle of confocal line detection only works well if the center of the illumination beam propagates parallel to the orientation of the slit detector (or of the line sensor); see Figs. 5(b) and 5(c). Even Bessel beams, which have been shown to be stable in their propagation directions in inhomogeneous media, are refracted and deflected by large refractive index jumps. Such pronounced index changes can occur especially at the entrance of a large scattering medium, such as small plants, embryos, or cellular spheroids. The effect of beam deflection on the efficiency of confocal line detection has been simulated. The results for the propagation of laterally displaced Bessel beams through a large sphere are shown for both the conventional mode and the confocal line mode in Fig. 6. Figure 6(b) illustrates the deflection of the Bessel beams at both the first and second spherical interfaces. Due to the Bessel beam's extended ring system the illumination intensity inside the sphere is homogeneous, although the optical sectioning is as bad as shown in Fig. 5(a). However, by applying confocal line detection as sketched by the slit in Fig. 6(b), the (fluorescence) intensity along the slit decays strongly. The decay of the detected intensity along z is stronger the more each single beam is deflected out of the slit area. This effect results in a rather inhomogeneous illumination intensity inside the large spherical object, as shown in Fig. 6(c).

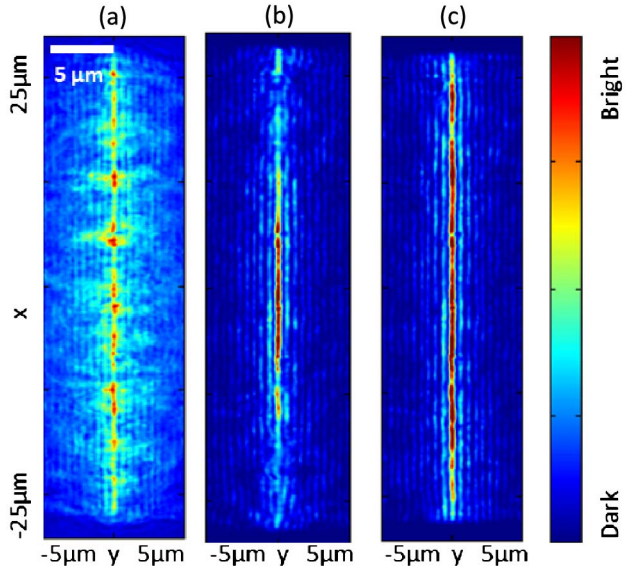

Fig. 5. Light-sheet intensities $p(x,y)$ located in the focal plane after 24 µm propagation through a cluster of spheres. (a) Bessel beam light sheet with conventional imaging, (b) Bessel beam light sheet using confocal line detection without phase correction, and (c) Bessel beam lightsheet using confocal line detection with phase correction.

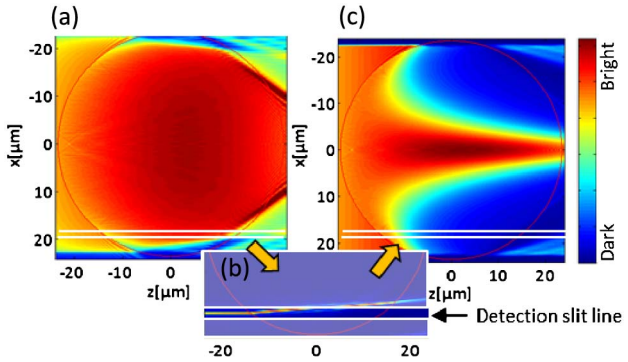

Fig. 6. Bessel beam light-sheet intensities $p(x,z)$ located in the focal plane while propagating through a large sphere. (a) Bessel beam light sheet with conventional imaging, (b) fluorescence is detected only along the straight line of the slit, and (c) Bessel beam light sheet using confocal line detection.

5. Geometric Phase Correction for Spherical Objects and Clusters

Following this, the evident idea is to tilt every single Bessel beam incident on the first interface, to make it propagate parallel to the detection slit after refraction at this interface. For our approach this requires several conditions to be fulfilled. First, the Bessel beam must be tilted by the SLM, as shown in Fig. 3. Second, the central lobe of the intensity distribution of the Bessel beam behaves similarly to a ray in geometrical optics, which refracts at interfaces according to Snell's law. Third, the angle of the Bessel beam exiting the spherical object with unknown refractive index and radius is measurable from the spectrum of outgoing angles.

This geometrical situation is illustrated in Fig. 7, where a ray is incident on the first interface with angle θ_1 and transmitted with angle θ_2 relative to the sphere's normal. At the second interface the ray is refracted again. The mean refractive index outside the spherical object is n_0, while the mean refractive index inside the object is $n_1 = n_0 + \delta n$. Using the paraxial approximation of the ray transfer matrices, we

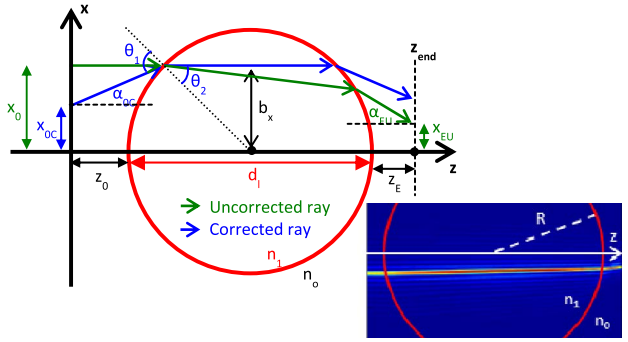

Fig. 7. Refraction according to Snell's law at both interfaces results in the green ray with exit angle α_{EU} and displacement x_{EU}. The corrected blue ray has an incident angle α_{0C} and an initial displacement with respect to the sphere center of x_{0C}. The inset in the lower right corner shows a simulation of the Bessel beam being refracted at the sphere surfaces.

obtain the following relation for the uncorrected incident beam with angle $\alpha_0 = 0$ and initial lateral beam displacement x_0

$$\begin{bmatrix} n_0\alpha_{EU} \\ x_{EU} \end{bmatrix} = \begin{bmatrix} 1 & 0 \\ z_E/n_0 & 1 \end{bmatrix} \times \begin{bmatrix} a_{11} & a_{12} \\ a_{21} & a_{22} \end{bmatrix} \times \begin{bmatrix} 1 & 0 \\ z_0/n_0 & 1 \end{bmatrix} \times \begin{bmatrix} 0 \\ x_o \end{bmatrix} \tag{6}$$

and

$$\begin{bmatrix} a_{11} & a_{12} \\ a_{21} & a_{22} \end{bmatrix} = \begin{bmatrix} 1-(\delta n/R)\cdot d_l/n_1 & -2(\delta n/R)+(\delta n/R)^2\cdot d_l/n_1 \\ d_l/n_1 & 1-(\delta n/R)\cdot d_l/n_1 \end{bmatrix}. \tag{7}$$

By knowing or measuring the axial distances z_0 and z_E and measuring α_{EU} and x_{EU}, it is possible to retrieve the unknown sphere radius R and mean refractive index n_1 of the specimen. For small beam displacements x_0, one can approximate $d_l \approx 2R$. From Eqs. (6) and (7) we find for the angle $\alpha_{EU} \approx x_0/n_0 \cdot (-2\delta n/R + 2\delta n^2/(n_1 R))$ and for the displacement $x_{EU} \approx z_E \cdot \alpha_{EU} + x_0[1-2\delta n/n_1]$. Solving for the unknown variables we find

$$n_1 \approx n_0 \cdot \frac{2x_0}{x_{EU} + x_0 - \alpha_{EU} z_E} = n_0 \cdot (1 + \delta n/n_0), \tag{8}$$

$$R \approx \frac{-2 \cdot \delta n \cdot x_0 \cdot z_E}{n_1(x_{EU} - x_0(1-2\delta n/n_1))}. \tag{9}$$

In principle, these parameters can be extracted from only one reference measurement for small x_0 as defined in Eqs. (8) and (9). In the case of the ideal sphere basically one measurement is sufficient. In the case of the sphere cluster typically the average of a few reference measurements should be taken in order to minimize scattering artifacts depending on the start position x_0 of the Bessel beam. Having estimated the radius and the mean refractive index of the large sphere or the cell cluster, it is easily possible to deduce the required tilt α_{0C} and start position x_{0C} of the Bessel beam.

The beam tilt enables a straight propagation inside the specimen and thereby an efficient use of the line-confocal principle. However, in order to obtain the desired displacement b_x inside the specimen, the corrected beam is also shifted with respect to the uncorrected one. The tilt angle α_{0C} can be obtained as follows:

$$\alpha_{0C} = \theta_1 - \theta_2 = \sin^{-1}\left(\frac{n_1}{n_0}\frac{b_x}{R}\right) - \sin^{-1}\left(\frac{b_x}{R}\right). \tag{10}$$

The new start position of the beam with respect to the center of the sphere reads (see Fig. 7):

$$x_{0C} = b_x - \left(R + z_0 - \sqrt{R^2 - b_x^2}\right) \cdot \tan\,\alpha_{0C}. \quad (11)$$

6. Recovering the Phase behind a Spherical Specimen

As sketched in Fig. 1, we exploit the interference between the Bessel beam propagating through the medium and a Gaussian reference beam. The electric field of the Bessel beam obtains an additional phase due to scattering and refraction, such that the electric field for each incident beam displacement $x_0 = b_x$ and behind the object at $z = z_{\text{end}}$ can be written as

$$\begin{aligned} E_B(x,y,z_{\text{end}},b_x) = {} & E_{0B}(x,y,z_{\text{end}},x_0) \\ & \cdot \exp(i\phi_B(x,y,x_0)) \\ & \cdot \exp(i\phi_{\text{def}}(x,y,z_{\text{end}},x_0)). \end{aligned} \quad (12)$$

Here ϕ_B is the conical phase of an ideal Bessel beam and the ϕ_{def} describes the phase change due to beam deflection and scattering. In our case we shift the phase of the Bessel beam by $\phi_{B,j} = j \cdot \pi/2 (j = 0,1,2,3)$ relative to the Gaussian beam by either the SLM or a piezo-driven mirror such that

$$E_{B,j}(x,y,z_{\text{end}},b_x) = E_B(x,y,z_{\text{end}},b_x) \cdot \exp(i\phi_{B,j}). \quad (13)$$

With the field of the Gaussian beam $E_G(x,y,z_{\text{end}}) = E_{0G}(x,y)\exp(i\phi_G)$ the resulting interference intensity at the position of the $\text{CAM}_{\text{trans}}$ thus reads

$$\begin{aligned} I_{\text{tot},j}(x,y,b_x) = {} & I_{0B}(x,y,b_x) + I_{0G}(x,y) \\ & + 2\sqrt{I_{0B}I_{0G}}\,\cos(\Delta\phi_j(x,y,b_x)). \end{aligned} \quad (14)$$

By using the principles of phase-shifting interferometry [16], it is straightforward to extract the phase $\phi_{\text{def}}(x,y,b_x)$ and the approximate mean k-vector $\mathbf{k}(b_x) \sim \int \nabla\phi_{\text{def}}(x,y,b_x)\text{d}x\text{d}y$ of the Bessel beam behind the object at $z = z_{\text{end}}$. To illustrate this concept, Fig. 8 displays four different interference intensities according to Eq. (14) and the retrieved phase $\phi_{\text{def}}(x,y,b_x)$ for a Bessel beam displaced by b_x. Alternatively, the mean k-vector and mean propagation angle of the exiting Bessel beam can be determined by free-space backpropagation of the field $E_B(x,y,z_{\text{end}},b_x)$.

7. Results

By applying the procedure described in the previous sections, we can correct each incident angle of each displaced Bessel beam, such that all beams propagate in parallel through the specimen. Thereby significantly more fluorescence light is collected when applying the confocal line detection principle. The potential of this beam correction method is demonstrated by the results shown in Fig. 9(a), where the uncorrected Bessel beams lead to an inhomogeneous

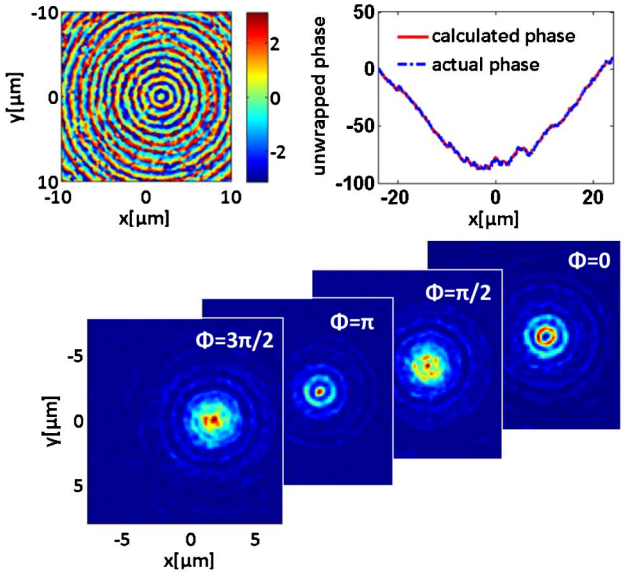

Fig. 8. Retrieval of the mean k vector from the distorted 2D phase $\phi_{\text{def}}\ (x,y,b_x)$. Four phase-shifted interference patterns were obtained behind the spherical cell cluster. The retrieved phase $\phi_{\text{def}}\ (x,0,b_x)$ is shown in 1D for the wrapped case. This phase allows to determine the exit angle of the beam and correction for the incident beam angle.

object illumination. In contrast, by applying the feedback phase correction algorithm the large sphere is homogeneously illuminated [Fig. 9(b)] and allows thin sectioning as shown in Fig. 5(c). The sphere radius and refractive index estimated from the refraction of one reference beam according to the procedure described in Section 5 is $R_{\text{est}} = 23.53$ µm and $n_{\text{est}} = 1.40$. It shows a very good agreement with the actual values of $R = 23.50$ µm and $n = 1.41$.

The algorithm works equally well for the nonhomogeneous cell cluster as displayed in Fig. 10(b). In this case the radius of the cell cluster and its average refractive index have been estimated from the propagation of four reference beams, resulting in $R_{\text{est}} = 23.52$ µm and $n_{\text{est}} = 1.40$. Again these values are in good agreement with the actual radius $R = 23.50$ µm and average index $n_{\text{avg}} = 1.38$. The intensity variations inside the specimen result from the scattering of light at the thousands of cells and thereby can

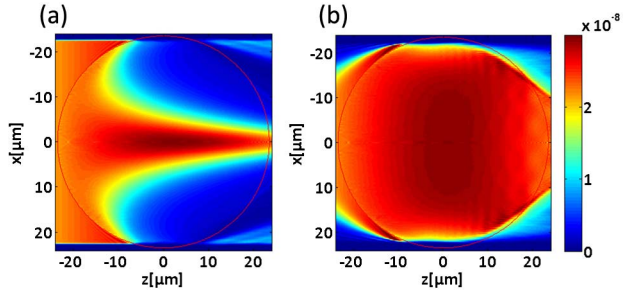

Fig. 9. Confocal line light-sheet intensities $p_{\text{CL}}\ (x,z)$ located in the focal plane while propagating through a large sphere. (a) Without phase correction and (b) with phase correction.

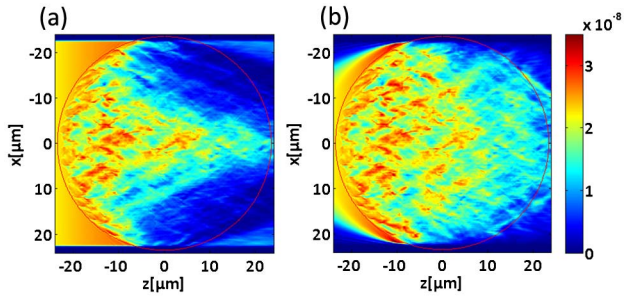

Fig. 10. Confocal line light-sheet intensities $p_{CL}(x,y)$ located in the focal plane while propagating through a cell cluster. (a) Without phase correction and (b) with phase correction.

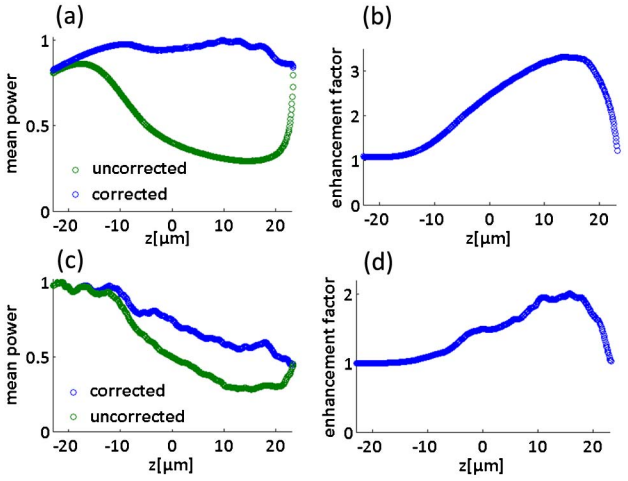

Fig. 11. Average decay of the detected fluorescence along the propagation direction for (a) a large sphere, and (c) a cell cluster. Enhancement factor of the feedback phase correction for (b) the case of the large sphere, and (d) the case of the cell cluster.

reveal internal structures of the specimen depending on the imaging process.

The increase in imaging efficiency due to our feedback phase correction is shown quantitatively by the average fluorescence decay along the propagation axis for the large sphere in Fig. 11(a) and for the cell cluster in Fig. 11(c). Each graph displays two averaged intensity profiles for the corrected and uncorrected case of the confocal line imaging mode. A strong improvement in the signal homogeneity up to 330% for the large sphere and 200% for the cell cluster is clearly visible in Figs. 11(b) and 11(d), respectively.

8. Discussion and Conclusion

We have performed a feasibility study for a feedback phase correction algorithm to improve the image quality in microscopy with self-reconstructing beams. In particular we have applied the BPM to simulate a realistic illumination inside large spherical specimens, such as multicellular spheroids, plants, or embryos. We have demonstrated by computer simulations that laterally scanned Bessel beams in combination with confocal line detection result in very thin light sheets revealing excellent optical sectioning. However, due to beam refraction and deflection at the interfaces of the spherically shaped specimens, the beams do not propagate parallel to the detection slit, thus degrading the specimen illumination and the image quality. By measuring the exit angle of the transmitted beam behind the specimen using phase-shifting interferometry, we could correct for the incident angle and hence for the propagation direction inside the specimen. Alternatively one could measure the beam's exit angle by the shift of the ring spectrum. However, for more complicated phase corrections of the Bessel beam, a 2D phase retrieval is more advantageous. The homogeneity of the illumination and fluorescence detection could be greatly improved for both the simple model of a large sphere and for the more advanced model of a cluster of shell-like spheres.

We could show by our simulations that a Bessel beam with its cone-like spectrum of k-vectors can be approximated as a ray even after refraction at a spherical interface. Based on this result, we have used the paraxial approximation of the ray transfer matrix to establish a relation between the incident angle and the exit angle. By taking only a few reference measurements in the central part of the specimen, its radius and mean refractive index could be retrieved with remarkable precision. With these two parameters we were able to correct for the incident beam angle from the exit beam angle, leading to very satisfying imaging results with a signal enhancement of 200%–300% in the back part of the image. This method can be extended to other geometric shapes, such as elongated spheres or cylinders, resulting in different Eqs. (8)–(11).

In our computer simulations we have designed the presented system to be realistic, such that in the near future it can be repeated in a real experiment using a new generation of light-sheet-based microscopes equipped with SLMs and the possibility of a fast phase readout. This will in principle enable the correction of the phase and thereby the illumination for each incident beam and each position inside the specimen.

This work was funded by the German Federal Ministry of Education and Research (BMBF).

References

1. H. Siedentopf and R. Zsigmondy, "Über Sichtbarmachung und Größenbestimmung ultramikroskopsicher Teilchen," Ann. Phys. **10**, 1 (1903).
2. J. Huisken, J. Swoger, F. Del Bene, J. Wittbrodt, and E. H. K. Stelzer, "Optical sectioning deep inside live embryos by selective plane illumination microscopy," Science **305**, 1007–1009 (2004).
3. A. Rohrbach, "Artifacts resulting from imaging in scattering media: a theoretical prediction," Opt. Lett. **34**, 3041–3043 (2009).
4. F. O. Fahrbach, P. Simon, and A. Rohrbach, "Microscopy with self-reconstructing beams," Nat. Photonics **4**, 780–785 (2010).
5. T. A. Planchon, L. Gao, D. E. Milkie, M. W. Davidson, J. A. Galbraith, C. G. Galbraith, and E. Betzig, "Rapid three-dimensional isotropic imaging of living cells using Bessel beam plane illumination," Nat. Methods **8**, 417–423 (2011).

6. F. O. Fahrbach and A. Rohrbach, "A line scanned light-sheet microscope with phase shaped self-reconstructing beams," Opt. Express **18**, 24229–24244 (2010).
7. E. Baumgart and U. Kubitscheck, "Scanned light sheet microscopy with confocal slit detection," Opt. Express **20**, 21805–21814 (2012).
8. L. Silvestri, A. Bria, L. Sacconi, G. Iannello, and F. S. Pavone, "Confocal light sheet microscopy: micron-scale neuroanatomy of the entire mouse brain," Opt. Express **20**, 20582–20598 (2012).
9. F. O. Fahrbach and A. Rohrbach, "Propagation stability of self-reconstructing Bessel beams enables contrast-enhanced imaging in thick media," Nat. Commun. **3**, 632 (2012).
10. P. J. Keller, A. D. Schmidt, J. Wittbrodt, and E. H. K. Stelzer, "Reconstruction of zebrafish early embryonic development by scanned light sheet microscopy," Science **322**, 1065–1069 (2008).
11. C. Lorenzo, C. Frongia, R. Jorand, J. Fehrenbach, P. Weiss, A. Maandhui, G. Gay, B. Ducommun, and V. Lobjois, "Live cell division dynamics monitoring in 3D large spheroid tumor models using light sheet microscopy," Cell Div. **6**, 22 (2011).
12. A. Maizel, D. von Wangenheim, F. Federici, J. Haseloff, and E. H. K. Stelzer, "High-resolution live imaging of plant growth in near physiological bright conditions using light sheet fluorescence microscopy," Plant J. **68**, 377–385 (2011).
13. M. D. Feit and J. A. Fleck, "Light propagation in graded index optical fibers," Appl. Opt. **17**, 3990–3998 (1978).
14. F. O. Fahrbach, V. Gurchenkov, K. Alessandri, P. Nassoy, and A. Rohrbach, "Light-sheet microscopy in thick media using scanned Bessel beams and two-photon fluorescence excitation," Opt. Express **21**, 13824–13839 (2013).
15. F. O. Fahrbach, V. Gurchenkov, K. Alessandri, P. Nassoy, and A. Rohrbach, "Self-reconstructing sectioned Bessel beams offer submicron optical sectioning for large fields of view in light-sheet microscopy," Opt. Express **21**, 11425–11440 (2013).
16. M. K. Kim, "Principles and techniques of digital holographic microscopy," SPIE Rev. **1**, 018005 (2010).